Volume 17
Number 31
21 August 2025
Pages 17865-18394

Nanoscale

rsc.li/nanoscale

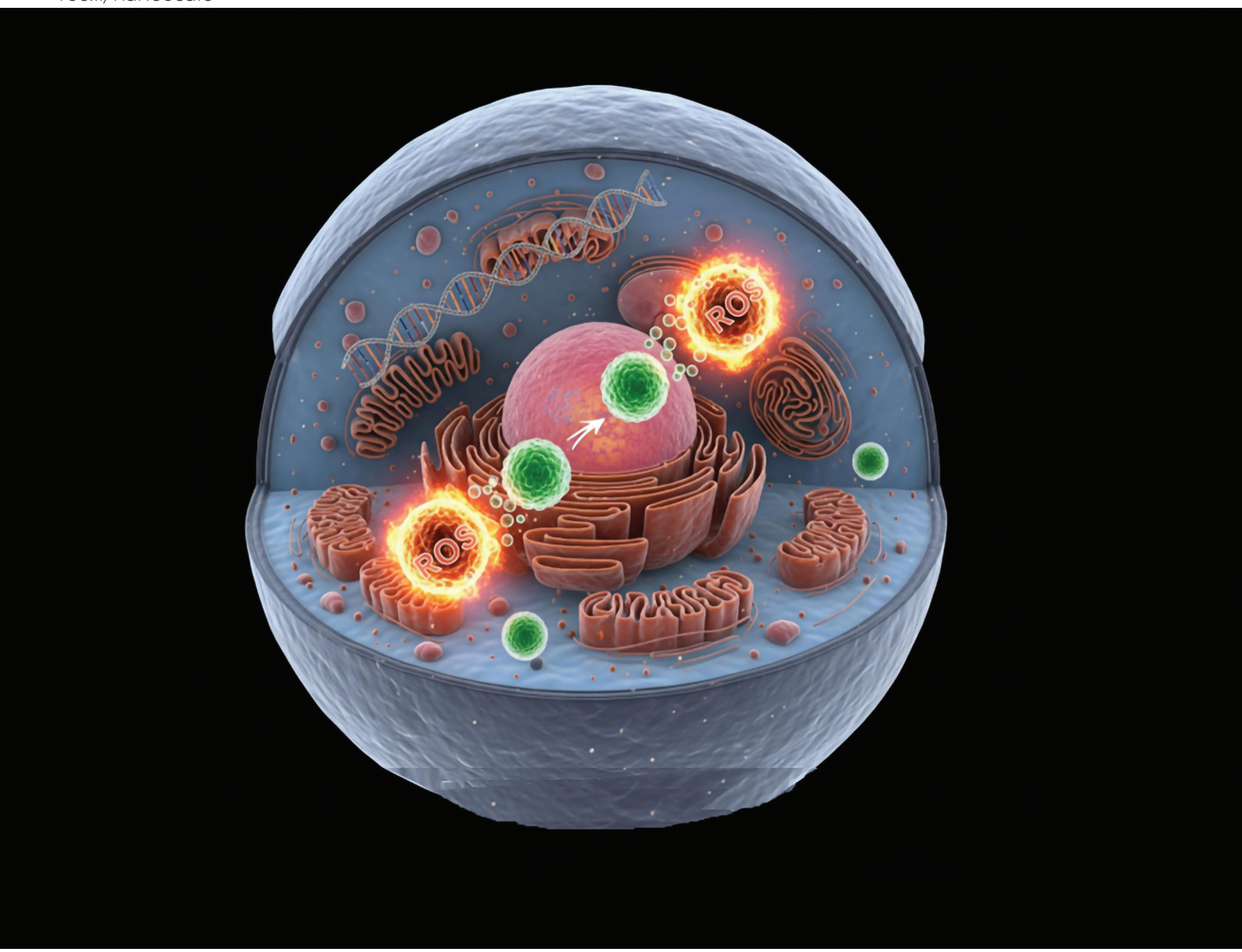

ISSN 2040-3372

ROYAL SOCIETY OF CHEMISTRY

COMMUNICATION
Sanjay Singh *et al.*
CeO_2- and Mn_3O_4-based nanozymes exhibit scavenging of singlet oxygen species and hydroxyl radicals

NCNST

Nanoscale

ROYAL SOCIETY OF CHEMISTRY

COMMUNICATION

View Article Online
View Journal | View Issue

Cite this: *Nanoscale*, 2025, **17**, 18077

Received 29th January 2025,
Accepted 24th April 2025

DOI: 10.1039/d5nr00430f

rsc.li/nanoscale

CeO_2- and Mn_3O_4-based nanozymes exhibit scavenging of singlet oxygen species and hydroxyl radicals†

Krishnendu M. R.,[a,b] Divya Mehta[a,b] and Sanjay Singh *[a,b]

Singlet oxygen and hydroxyl radicals are highly reactive species that contribute significantly to oxidative stress-related pathologies. Herein, we report the effective scavenging of $^1O_2$ and $^{\bullet}OH$ by CeO_2- and Mn_3O_4-based nanozymes and compare them with the well-known scavengers of these radicals. The IC_{50} values of scavenging of $^{\bullet}OH$ by these nanozymes were compared with NAC, which were in the order of Mn_3O_4 [2.3 μM] < CeO_2 [5.4 μM] < NAC [28.4 μM]. Similarly, the IC_{50} values for $^1O_2$ scavenging were in the order of Mn_3O_4 [4.75 μM] < sodium azide [60.5 μM] < CeO_2 [857.27 μM]. The cell viability assays, ROS generation studies and cell cycle analysis revealed that these nanozymes (1 μg mL^{-1}) are biocompatible with mammalian cells.

Reactive oxygen species (ROS) generated through the chemical, photochemical, or biochemical reduction of oxygen are redox active intermediates that trigger a series of oxidative reactions.[1] Among various ROS, superoxide anions ($O_2^{\bullet-}$), hydroxyl radicals ($^{\bullet}OH$), singlet oxygen ($^1O_2$), and hydrogen peroxide (H_2O_2) are well known to orchestrate various biochemical reactions in mammalian cells/tissues. Overproduction of these ROS causes oxidation of various biological macromolecules, leading to critical ailments such as cancer, cardiovascular and neurodegenerative diseases, *etc*. Various non-invasive cancer treatment strategies such as photothermal, photodynamic, and sonodynamic therapies involve the generation of excessive ROS for localized damage of cancer tissues.[2–4] Nanozymes have also been utilized as oxygen-independent radiodynamic therapeutics and also as pro-drugs for the treatment of various diseases.[5,6] Several synthetic scavengers, such as corticosteroids and nonsteroidal anti-inflammatory drugs, have been used to alleviate the toxic effects of ROS; however, they cause gastrointestinal and cardiovascular complications and renal failure.[7] Recently, antioxidant nanozymes such as cerium oxide (CeO_2 NPs) and manganese oxide (Mn_3O_4 NPs) and derivatives of fullerenes have been discovered to scavenge the extremely reactive and harmful $O_2^{\bullet-}$ and H_2O_2.[8,9] Although a lot of effort has been made to develop scavengers of $O_2^{\bullet-}$ and H_2O_2, limited attention is given to $^{\bullet}OH$ and $^1O_2$ scavenging. These radicals are particularly significant due to their extreme reactivity and potential for causing severe cellular damage, leading to various diseases.

The well-explored methods of $^{\bullet}OH$ generation are the Fenton and Haber–Weiss reactions, which contribute to various pathologies, including liver damage in obstructive jaundice, ascites syndrome, familial amyotrophic lateral sclerosis (FALS), and ischemia-induced intestinal vascular permeability.[10–13] $^1O_2$, an electronically excited form of oxygen, plays a key role in oxidative stress, particularly in conditions like acute endotoxemia and type 2 diabetes, leading to impaired glucose tolerance and insulin resistance.[14,15] Given the strong oxidizing nature of $^{\bullet}OH$ and $^1O_2$, it is highly desirable to develop materials that can effectively scavenge these radicals from biological systems to prevent oxidative damage. CeO_2 and Mn_3O_4 NPs have been extensively studied for their antioxidant properties to scavenge ROS, such as $O_2^{\bullet-}$ and H_2O_2. However, there are fewer reports on scavenging $^{\bullet}OH$ and $^1O_2$ by nanozymes. Reported methods for nanozyme-mediated ROS scavenging often rely on complex processes of radical generation or detection, exhibit limited efficiency, and are effective under acidic conditions.[16–18] Additionally, scavengers of $^1O_2$ such as sodium azide (NaN_3) raise toxicity concerns due to the inhibition of metalloenzymes,[19] while $^{\bullet}OH$ scavenging polyamines require relatively high concentrations to achieve effective neutralization.[20] These limitations highlight the need for developing biocompatible and efficient nanozymes capable of scavenging reactive species under physiologically relevant conditions. Herein, we report the synthesis of dextran-coated CeO_2 and Mn_3O_4 NPs/nanozymes that are biocompatible and efficient at scavenging $^{\bullet}OH$ and $^1O_2$. We report novel methods to generate these radicals and employ multiple independent

[a]*Nanobiology and Nanozymology Research Laboratory, National Institute of Animal Biotechnology (NIAB), Opposite Journalist Colony, Near Gowlidoddy, Extended Q-City Road, Gachibowli, Hyderabad, Telangana 500032, India. E-mail: sanjay@niab.org.in*

[b]*Regional Centre for Biotechnology (RCB), Faridabad 121001, Haryana, India*

† Electronic supplementary information (ESI) available. See DOI: https://doi.org/10.1039/d5nr00430f

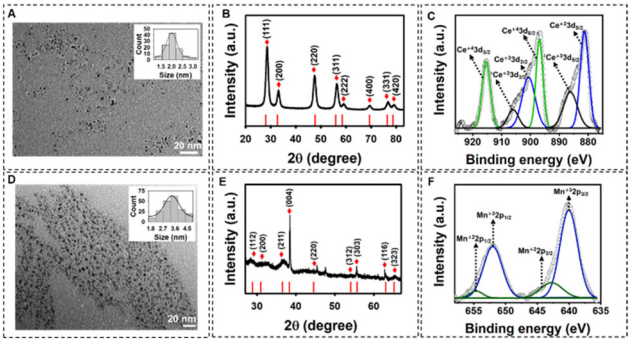

Fig. 1 Characterization of Dex-CeO_2 NPs and Dex-Mn_3O_4 NPs: (A) TEM image (inset shows particle size distribution), (B) XRD pattern and (C) XPS spectra of Dex-CeO_2 NPs. (D) TEM image (inset shows particle size distribution), (E) XRD pattern and (F) XPS spectra of Dex-Mn_3O_4 NPs.

experiments to confirm the scavenging capabilities of these nanozymes and propose the possible reaction mechanisms.

Dextran-coated cerium oxide nanoparticles (Dex-CeO_2 NPs) and manganese oxide nanoparticles (Dex-Mn_3O_4 NPs) were characterized by several advanced techniques. FTIR spectra revealed characteristic transmissions at 450 cm^{-1} and 1380 cm^{-1} for Dex-CeO_2 NPs, corresponding to Ce–O stretching and vibrational modes (Fig. S1A†),[21] while Dex-Mn_3O_4 NPs showed signals at 519 and 613 cm^{-1}, corresponding to Mn–O and Mn–O–Mn bond vibrations (Fig. S2A†).[22] The UV-Vis spectra of both nanoparticles showed a peak at 290 nm, confirming the dextran coating (Fig. S1B and S2B†). TEM analysis revealed that Dex-CeO_2 NPs have an average size of ~2 nm (Fig. 1A), while Dex-Mn_3O_4 NPs were ~3 nm in diameter (Fig. 1D). XRD analysis of Dex-CeO_2 NPs showed diffraction peaks matching the CeO_2 fluorite structure (JCPDS file no. 34-0394) (Fig. 1B). XRD analysis confirmed the tetragonal phase of Mn_3O_4 (JCPDS file no. 24-0734) (Fig. 1E). XPS analysis of Dex-CeO_2 NPs revealed the presence of both Ce^{3+} and Ce^{4+} states. The Ce 3d core-level spectrum for Ce^{4+} was deconvoluted into a single spin–orbit pair (915.25 eV and 896.85 eV), while Ce^{3+} exhibited two spin–orbit pairs (900.75 eV/881.4 eV and 906.00 eV/886.18 eV) representing $3d_{3/2}$ and $3d_{5/2}$, respectively (Fig. 1C).[23] The integrated area under the two spin–orbit pairs of Ce^{3+} and the single spin–orbit pair of Ce^{4+} was used to calculate the Ce^{3+}/Ce^{4+} ratio and *vice versa*[24,25] (Table S1†). The following equations were used for the calculation of $[Ce^{3+}]$:

$$[Ce^{3+}] = \frac{[ACe^{3+}3d_{5/2} + ACe^{3+}3d_{3/2} + A'Ce^{3+}3d_{5/2} + A'Ce^{3+}3d_{3/2}]}{[ACe^{3+}3d_{5/2} + ACe^{3+}3d_{3/2} + A'Ce^{3+}3d_{5/2} + A'Ce^{3+}3d_{3/2} + ACe^{4+}3d_{5/2} + ACe^{4+}3d_{3/2}]}$$

and $[Ce^{4+}]$:

$$[Ce^{4+}] = \frac{[ACe^{4+}3d_{5/2} + ACe^{4+}3d_{3/2}]}{[ACe^{3+}3d_{5/2} + ACe^{3+}3d_{3/2} + A'Ce^{3+}3d_{5/2} + A'Ce^{3+}3d_{3/2} + ACe^{4+}3d_{5/2} + ACe^{4+}3d_{3/2}]}$$

where A is the integrated area under each deconvoluted peak.

Based on this calculation, the concentration of $[Ce^{3+}]$ and $[Ce^{4+}]$ was found to be 0.65 and 0.35, respectively. The O 1s core spectrum of Dex-CeO_2 NPs was deconvoluted into two peaks at 531.6 eV and 530.50 eV, corresponding to surface oxygen and lattice oxygen, respectively (Fig. S1C†). The high-resolution C 1s spectrum was also deconvoluted into two peaks with binding energies at 284.65 eV and 285.8 eV, which are attributed to C–C and C–OH bonds, respectively (Fig. S1D†). In Dex-Mn_3O_4 NPs, the Mn 2p core spectrum was deconvoluted into two spin–orbit pairs of $2p_{3/2}/2p_{1/2}$ at 640.10 eV/651.93 eV and 642.86 eV/654.64 eV, indicating mixed Mn^{2+} and Mn^{3+} valence states, respectively (Fig. 1F).[26] The O 1s spectrum of Dex-Mn_3O_4 NPs revealed peaks at 530.48 eV and 531.85 eV, corresponding to Mn–OH and H–O–H bonds (Fig. S2C†). Additionally, the high-resolution C 1s spectrum was deconvoluted into three peaks at 284.72, 285.95, and 286.51 eV which were identified as corresponding to C–C/C=C, C–O–C, and C=O bonds, respectively (Fig. S2D†). EDX analysis of both the nanoparticles showed prominent signals for carbon (C), oxygen (O), and the respective elements, Ce or Mn, with characteristic energy lines, Ce (0.88 and 4.84 keV) and Mn (5.8 and 0.6 keV), confirming the elemental composition (Fig. S1E and S2E†). Elemental mapping of Dex-CeO_2 NPs displayed distinct signals for Ce and O, with an overlay indicating the oxide of cerium, while the overlapping signals of Mn and O suggested a strong Mn–O interaction and thus the presence of Mn oxide (Fig. S1F and S2F†).[27,28]

The typical Fenton reaction, involving oxidation of H_2O_2 by the ferrous ions (Fe^{2+}), was utilized to generate $^{\bullet}OH$[29] (Fig. S3A†). The high affinity of $^{\bullet}OH$ with a specific fluorescent probe, terephthalic acid (TA), was used to probe the generation of the former. The so-generated fluorescent product, 2-hydroxyterephthalic acid, could be easily monitored by following the Ex./Em. at 320/425 nm. The reaction of $FeSO_4$ with H_2O_2 in the presence of TA showed the maximum emission intensity (Fig. 2A, black curve), due to the formation of 2-hydroxyterephthalic acid, suggesting the possible formation of $^{\bullet}OH$. To this suspension, the addition of increasing concentrations of Dex-CeO_2 NPs (25–200 μM) and Dex-Mn_3O_4 NPs (25–200 μM) caused a decrease in the emission intensity of terephthalic acid (Fig. S3B and S3C†). Furthermore, the scavenging kinetics of $^{\bullet}OH$ by the nanozymes were followed for 20 minutes. The results revealed that with the increase in the concentration of the nanozymes, there was a concomitant decrease in the TA emission intensity at 425 nm (Fig. 2A and B). These results indicate that Dex-CeO_2 NPs and Dex-Mn_3O_4 NPs could effectively scavenge $^{\bullet}OH$ even in the event of constant generation of $^{\bullet}OH$, typically apparent during the biochemical reactions in mammalian cells. The possibility of TA oxidation by H_2O_2

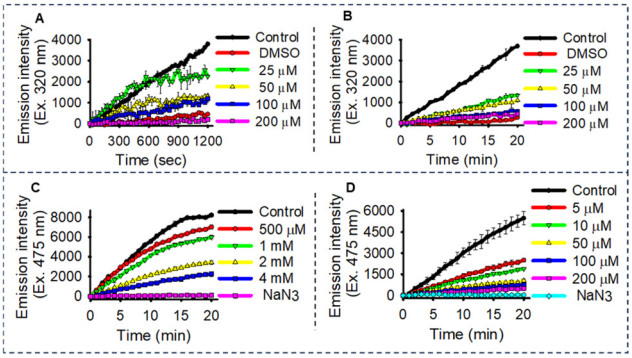

Fig. 2 Reaction kinetics of $^{\bullet}OH$ scavenging by different concentrations of (A) Dex-CeO_2 NPs and (B) Dex-Mn_3O_4 NPs with the control as $FeSO_4$ + H_2O_2 + TA. Scavenging of $^1O_2$ by different concentrations of (C) Dex-CeO_2 NPs and (D) Dex-Mn_3O_4 NPs with the control as HRP + H_2O_2 + SOSG. All the experiments were performed at least thrice in triplicate and the data are plotted with the standard deviation.

alone (without $^{\bullet}OH$ radicals) was tested using two methods, by substituting $FeSO_4$ (Fe^{2+}) with $FeCl_3$ (Fe^{3+}) in the Fenton reaction system and direct exposure of TA to H_2O_2 (Fig. S4†). Both of these reactions failed to produce detectable TA oxidation, which suggests the requirement for Fe^{2+} in catalyzing $^{\bullet}OH$ generation *via* the Fenton reaction and rules out the possibility of false positive signals of TA oxidation by only H_2O_2.

A significant reduction in the emission intensity of 2-hydroxyterephthalic acid in presence of 10% DMSO (Fig. S5A and S5C†) and 10% ethanol (Fig. S5B and S5D†) relative to the control ($FeSO_4$ + H_2O_2 in a buffer) was observed to be analogous to 50 μM of Dex-CeO_2 NPs and Dex-Mn_3O_4 NPs.

The generation of $^1O_2$ was achieved by utilizing the catalytic reaction between horseradish peroxidase (HRP) and H_2O_2 at pH 6 in the presence of SOSG (Fig. S6A†), a selective fluorescent probe for $^1O_2$, due to the formation of SOSG-endoperoxide (SOSG-EP) (Ex./Em. = 475/530 nm). The reaction system used for $^1O_2$ generation consisted of HRP and H_2O_2 in a buffer at pH 6 (Fig. S6A,† black curve). NaN_3 was used as a scavenger of $^1O_2$. HRP, in the presence of H_2O_2, generates $O_2^{\bullet-}$, which serves as a source of $^1O_2$ after oxidation. In a study by Ingenbosch *et al.*, the catalytic reaction between HRP and H_2O_2 was carried out in the presence of the superoxide dismutase (SOD) enzyme, a known $O_2^{\bullet-}$ scavenger. Although the SOSG-EP fluorescence decreased with increasing SOD concentration, there was no complete quenching of the fluorescence, indicating the major role of $O_2^{\bullet-}$ in $^1O_2$ formation. We also tested the hypoxanthine/xanthine oxidase system, known to generate $O_2^{\bullet-}$, using SOSG at pH 6, but it did not show significant emission at 530 nm, indicating the absence of $^1O_2$ (Fig. S6B,† red curve). Using DHE, a probe for $O_2^{\bullet-}$ detection, we observed no emission in the presence of *p*-benzoquinone ($O_2^{\bullet-}$ inhibitor) and no decrease in emission intensity in the presence of NaN_3, suggesting that the hypoxanthine/xanthine oxidase system only produced $O_2^{\bullet-}$ and no $^1O_2$ (Fig. S6C†). Subsequently, we also tested the formation of $O_2^{\bullet-}$ in the HRP and H_2O_2 system and compared it with the hypoxanthine/xanthine oxidase system using DHE (Fig S6D†). DHE showed excellent emission when incubated with hypoxanthine/xanthine oxidase; however, HRP + H_2O_2 with DHE showed weak emission intensity. This observation suggests that the HRP + H_2O_2 reaction produces predominantly $^1O_2$ with a minor population of $O_2^{\bullet-}$, possibly contributing to the formation of $^1O_2$ in the system. The $^1O_2$ scavenging potential of Dex-CeO_2 NPs and Dex-Mn_3O_4 NPs was estimated by following the fluorescence emission spectra of SOSG-EP at 530 nm (Fig. S7A†). The control reaction consisting of HRP and H_2O showed strong emission intensity (Fig. S7B and S7C,† black curve). In the presence of Dex-CeO_2 NPs (500 μM–4 mM) and Dex-Mn_3O_4 NPs (5–200 μM), the emission intensity of SOSG-EP was observed to decrease in a concentration-dependent manner, which suggests the successful scavenging of $^1O_2$ by the nanozymes (Fig. S7B and S7C†). A similar trend of inhibition of $^1O_2$ could be seen at various concentrations of Dex-CeO_2 NPs (500 μM–4 mM) and Dex-Mn_3O_4 NPs (5–200 μM) for a 20-minute kinetics study, which further validates their scavenging ability (Fig. 2C and D). Dex-Mn_3O_4 NPs possess stronger $^1O_2$ scavenging potential (~20 times) than Dex-CeO_2 NPs, as evident from their extent of scavenging ability at lower concentrations (5–200 μM). A notable reduction in the emission intensity of SOSG-EP was observed in the presence of the inhibitors, NaN_3 (Fig. S8A and S8C†) and parabenzoquinone (Fig. S8B and S8D†), relative to the control group (HRP and H_2O_2 in buffer). This is analogous to the inhibitory effects of Dex-CeO_2 NPs (1 mM) and Dex-Mn_3O_4 NPs (10 μM).

The possible byproducts generated by the scavenging of $^{\bullet}OH$ could be H_2O_2 and O_2. Therefore, we tested the supernatant of the Fenton reaction system, employed for studying the scavenging activity of NPs, and estimated the generation of H_2O_2 by the Amplex Red assay. The generation of molecular oxygen was estimated using an oxygen-sensitive probe. The $^{\bullet}OH$ scavenging by CeO_2 NPs neither displayed the formation of molecular oxygen nor H_2O_2 (Fig. 3A, B, and S9A†), which indicates that $^{\bullet}OH$ is being catalytically converted into H_2O possibly by the following reaction: [Ce_2O_3 (Ce^{3+}) + 2($^{\bullet}OH$) → 2CeO_2 (Ce^{4+}) + H_2O]. A similar observation has been reported by Xue *et al.*[30] Thus, the observed scavenging activity of CeO_2 NPs could be well correlated with the unique ability to switch between their dual oxidation states Ce^{3+} and Ce^{4+}. The relatively higher concentration of Ce^{3+} at the surface of CeO_2 NPs acts as the active sites for the redox reaction and allows them to react with the powerful oxidant, $^{\bullet}OH$, by reversibly switching between the Ce^{3+} and Ce^{4+} ions.[31] Interestingly, the $^{\bullet}OH$ scavenging by Dex-Mn_3O_4 NPs showed significant liberation of O_2 at higher concentrations (200 μM) (Fig. 3C) than at lower concentrations (100 μM). Additionally, the Amplex Red test showed stronger absorbance at 570 nm at both the concentrations of Dex-Mn_3O_4 NPs (100 μM and 200 μM) compared to the control ($FeSO_4$ and H_2O_2). These observations indicate the formation of H_2O_2 in the reaction system (Fig. 3D and S9B†). These experimental results indicate that H_2O_2 may form as a byproduct during the $^{\bullet}OH$ scavenging activity of Dex-Mn_3O_4 NPs. However, at higher concentrations of Dex-Mn_3O_4 NPs, the

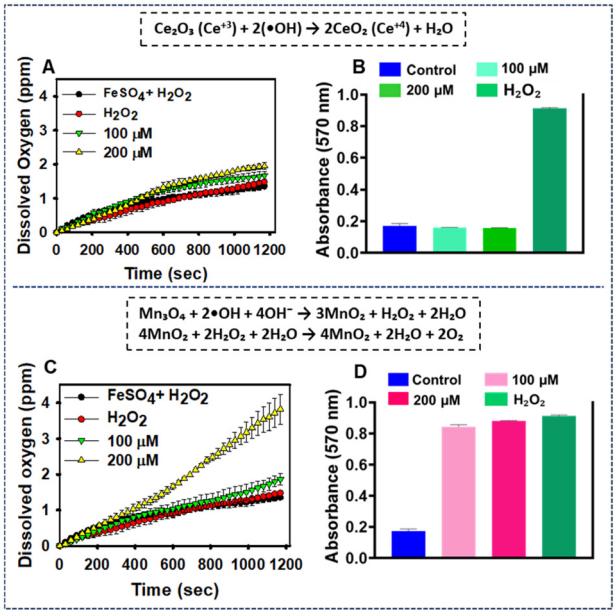

Fig. 3 Possibility of conversion of $^{\bullet}OH$ into O_2 or H_2O_2 by nanozymes: Conversion of $^{\bullet}OH$ into dissolved oxygen (A) and H_2O_2 (B) by Dex-CeO_2 NPs. Conversion of $^{\bullet}OH$ into dissolved oxygen (C) and H_2O_2 (D) by Dex-Mn_3O_4 NPs. Detection of H_2O_2 formation was performed using the Amplex Red assay whereas dissolved oxygen was measured using a DO meter. All the experiments were performed three times independently and the data are plotted with the standard deviation.

generated H_2O_2 could auto-degrade into O_2 and H_2O as evidenced by the generation of O_2 at 200 μM of Dex-Mn_3O_4 NPs (Fig. 3C). The probable reaction mechanism for the $^{\bullet}OH$ scavenging activity of Dex-Mn_3O_4 NPs can be represented as follows:

$$Mn_3O_4 + 2{}^{\bullet}OH + 4OH^- \rightarrow 3MnO_2 + H_2O_2 + 2H_2O \quad \text{(at low Mn concentrations)}$$

$$4MnO_2 + 2H_2O_2 + 2H_2O \rightarrow 4MnO_2 + 2H_2O + 2O_2 \quad \text{(at high Mn concentrations)}$$

Thus, both the nanozymes follow different reaction mechanisms to scavenge $^{\bullet}OH$ at physiological pH.

Furthermore, the mechanism for $^1O_2$ scavenging by Dex-CeO_2 and Dex-Mn_3O_4 NPs could possibly involve a series of redox reactions, with the formation of $O_2^{\bullet-}$ as an intermediate species and O_2 as the end product. During the initial steps, the nanozymes act as electron donor to $^1O_2$, facilitating its reduction into $O_2^{\bullet-}$.[32] This step is favoured by the half-reaction: $^1O_2 + e^- \rightarrow O_2^{\bullet-}$ (E° = +0.81 eV). In this step, Ce^{+3} atoms from CeO_2 NPs undergo redox switching to Ce^{4+} oxidation state as evidenced by the feasibility of the half-reaction, $Ce^{4+} + e^- \rightarrow Ce^{3+}$ (E° = +1.72 eV).[33] During the second course of reaction, Ce^{4+} is reduced to Ce^{3+} by the following reaction: $Ce^{4+} + O_2^{\bullet-} \rightarrow Ce^{3+} + O_2$. Korsvik *et al.* have proposed a similar mechanism for $O_2^{\bullet-}$ dismutation by CeO_2 NPs, analogous to the activities of Fe- and Mn-SODs.[25]

The overall redox reactions involving the $^1O_2$ scavenging mechanism of Dex-CeO_2 NPs can be summarized as:

$$5Ce^{3+} + {}^1O_2 \rightarrow 5Ce^{4+} + O_2^{\bullet-} \quad (1)$$

$$Ce^{4+} + O_2^{\bullet-} \rightarrow Ce^{3+} + O_2 \quad (2)$$

In the case of Mn_3O_4 NPs, the Mn^{2+} ions donate electrons to reduce $^1O_2$ to $O_2^{\bullet-}$ ($Mn^{2+} \rightarrow Mn^{3+} + e^-$ (E° = +1.509 eV)). Subsequently, the generated $O_2^{\bullet-}$ is converted back into O_2 *via* oxidation by the following reaction: $O_2^{\bullet-} \rightarrow O_2 + e^-$ (E° = +0.33 eV). This step involves electron transfer between $O_2^{\bullet-}$ and the nanozyme, resulting in the reduction of the nanozyme and regeneration of their oxidized state. Mn^{3+} is reduced back to Mn^{2+} by the following reaction: $Mn^{3+} + e^- \rightarrow Mn^{2+}$ (E° = +1.51 eV). The overall scavenging activity of the nanoparticle involves the reduction of $^1O_2$ to $O_2^{\bullet-}$, followed by the conversion of $O_2^{\bullet-}$ to O_2, thereby effectively neutralizing $^1O_2$.

The mechanism of $^1O_2$ scavenging by Dex-Mn_3O_4 NPs could be possibly written as:

$$5Mn^{2+} + {}^1O_2 \rightarrow 5Mn^{3+} + O_2^{\bullet-} \quad (3)$$

$$Mn^{3+} + O_2^{\bullet-} \rightarrow Mn^{2+} + O_2 \quad (4)$$

Learman *et al.* have experimentally demonstrated the role of $O_2^{\bullet-}$ as an effective oxidant of Mn^{2+}, promoting the formation of Mn^{3+} oxide. Mechanistically, the reaction was thought to proceed through the formation of a Mn^{3+} intermediate, thereby facilitating the oxidation of Mn^{2+} with concomitant scavenging of $^1O_2$.[34]

The IC_{50} values, representing the half-maximal inhibitory concentration, were determined for scavenging of both $^{\bullet}OH$ and $^1O_2$ by Dex-CeO_2 NPs (Fig. S10A, B and Fig S11A, B†) and Dex-Mn_3O_4 NPs (Fig. S10C, D and Fig S11C, D†) and compared with those of known scavengers, NAC for $^{\bullet}OH$ (Fig. S10E and F†) and NaN_3 for $^1O_2$ (Fig. S11E and F†). The results revealed that Dex-Mn_3O_4 NPs exhibited the best scavenging efficiency for both $^{\bullet}OH$ [2.3 μM] and $^1O_2$ [4.75 μM] compared to the well-known scavengers NAC [28.4 μM] and NaN_3 [60.5 μM] (Table S2†).

Furthermore, Dex-CeO_2 NPs also showed comparable scavenging of $^{\bullet}OH$ [5.4 μM] with those of Dex-Mn_3O_4 NPs [2.3 μM] and NAC [28.4 μM]; however, poor scavenging of $^1O_2$ [857.27 μM] compared to Dex-Mn_3O_4 NPs [4.75 μM] and NaN_3 [60.5 μM] was observed. Specifically, Dex-Mn_3O_4 NPs exhibited significantly lower IC_{50} values for both the radicals, indicating superior scavenging capabilities. Furthermore, Dex-CeO_2 NPs outperformed NAC in scavenging $^{\bullet}OH$; however, they were less efficient than Dex-Mn_3O_4 NPs.

CeO_2 NPs are well known for their ability to undergo reversible redox cycling between the Ce^{3+} and Ce^{4+} oxidation states, which is the mechanistic basis for their enzyme-mimetic functions.[35] We also tested the redox cycling behavior of Dex-CeO_2 NPs (Fig. S12H†) and compared that with bare CeO_2 NPs (Fig. S12G†). The colourless suspensions of bare CeO_2 NPs (Fig. S12G,† bottle 1) and Dex-CeO_2 NPs (Fig. S12H,† bottle 1)

developed into dark yellow suspensions immediately after H_2O_2 addition, indicating the oxidation of Ce^{3+} to Ce^{4+} (Fig. S12G,† bottle 2 and Fig. S12H,† bottle 2). Following incubation at 37 °C for 15 days, the suspensions reverted to the colourless state, confirming the regeneration of Ce^{3+} during the redox transition (Fig. S12G,† bottle 3 and Fig. S12H,† bottle 3). To evaluate the persistence of redox reversibility, H_2O_2 was again introduced into the regenerated colourless suspensions. A progressive development of the yellow colouration was again observed (Fig. S12G,† bottle 4 and Fig. S12H,† bottle 4), indicating a second oxidation cycle of conversion of Ce^{3+} into Ce^{4+}. This reversible colour change upon repeated H_2O_2 exposure provides strong evidence of sustained redox cycling by Dex-CeO_2 NPs under physiological conditions. We also investigated if the redox cycling of Dex-CeO_2 NPs affects their ability to scavenge $^{\bullet}OH$ and $^1O_2$ (Fig. S12A, B, C and D†). The $^{\bullet}OH$ and $^1O_2$ scavenging activity of Dex-CeO_2 NPs post-redox recycling showed no significant deviation in comparison with the respective controls. Results from UV-vis absorbance spectroscopy further support this observation as there was no appreciable change in the absorbance signal of bare CeO_2 NPs at 280–290 nm (Fig. S12E†) and Dex-CeO_2 NPs at 290 nm (Fig. S12F†) following redox cycling, indicating that the optical properties of the Dex-CeO_2 NPs remain unaltered throughout the process.

The *in vitro* biocompatibility assessment of Dex-CeO_2 NPs and Dex-Mn_3O_4 NPs was performed in intestinal epithelial (IEC-6) cells by incubating for 24, 48, and 72 hours with different concentrations (100 ng mL^{-1} – 1 μg mL^{-1}). The nanozymes demonstrated excellent stability in serum-free and serum-containing cell culture media (DMEM-F12). The nanozymes neither showed aggregation nor any significant decrease in $^{\bullet}OH$ and $^1O_2$ radical scavenging ability (Fig. S13A, B, C, D, E and F†). These results confirm the stability of dextran-coated nanozymes in physiologically relevant media. The MTT assay results showed no significant reduction in cell viability after exposure to Dex-CeO_2 NPs (Fig S14A†) and Dex-Mn_3O_4 NPs (Fig S14D†) for 24 and 48 hours. However, higher concentrations of Dex-Mn_3O_4 NPs (0.75 μg mL^{-1} and 1 μg mL^{-1}) caused an ~10–15% decrease in cell viability when incubated for 72 hours. This observation could be due to the deposition of Dex-Mn_3O_4 NPs (higher concentrations) on the cells, causing physical damage. The cell morphology revealed no significant alteration in the growth and adhesion pattern of typical IEC-6 cells when exposed to different concentrations of Dex-CeO_2 NPs (Fig. S15†) and Dex-Mn_3O_4 NPs (Fig. S16†). The cell cycle pattern analysis in a large population of IEC-6 cells exposed to Dex-CeO_2 NPs and Dex-Mn_3O_4 NPs indicated no significant alteration in the distribution of cell cycle phases (G1, S, and G2/M) compared to the control cells (Fig S14B and S14E†). Quantitative analysis revealed that the proportion of cells in each phase (G1, S, and G2/M) of the treated groups remained comparable to that of the control cells. This suggests that treatment with Dex-CeO_2 NPs (Fig S14C†) and Dex-Mn_3O_4 NPs (Fig S14F†) did not induce any notable changes in cell cycle progression or arrest at the tested concentrations. Furthermore, H_2DCFDA dye-based investigation of ROS generation by higher concentrations of Dex-CeO_2 NPs and Dex-Mn_3O_4 NPs was performed. Fluorescence microscopy imaging showed strong green fluorescence signals from the positive control (cells exposed to H_2O_2) (Fig. S14G†) compared to the untreated (control) cells (Fig. S14J†) and the Dex-CeO_2 NP- (Fig S14M–O†) and Dex-Mn_3O_4 NP (Fig. S14P–R†)-treated cells. Thus, from the *in vitro* cellular experiments, it may be concluded that the developed antioxidant nanozymes are biocompatible to mammalian cells and do not elicit any oxidative stress and toxicity even at high concentrations.

In conclusion, the developed nanozymes efficiently scavenge $^{\bullet}OH$ and $^1O_2$ in a concentration- and time-dependent manner. Dex-Mn_3O_4 NPs exhibited superior scavenging of $^{\bullet}OH$ and $^1O_2$ compared to Dex-CeO_2 NPs and other specific scavengers, NAC and NaN_3. Mechanistically, Dex-CeO_2 NPs neutralize $^{\bullet}OH$ directly to produce water, while Dex-Mn_3O_4 NPs convert $^{\bullet}OH$ into H_2O_2, subsequently breaking it into O_2. Additionally, both the nanozymes effectively neutralize $^1O_2$ by converting it into O_2. The developed nanozymes were found to be biocompatible as their exposure did not affect the cell viability and induce oxidative stress, and the cell cycle progression pattern was also unaffected. Considering the growing interest in utilizing nanozymes for clinical applications, particularly in the treatment of oxidative-stress-associated diseases, both CeO_2- and Mn_3O_4-based nanozymes would be promising candidates for therapeutic applications. Although the results from *in vitro* experiments indicate that the developed nanozymes are non-toxic to mammalian cells, the *in vivo* safety assessment remains to be studied in detail before these nanozymes are considered for clinical studies.

Data availability

The data supporting this article have been included as part of the ESI.†

Conflicts of interest

There are no conflicts to declare.

Acknowledgements

S. Singh thanks the NIAB Core Grant (C0046) for financial support. K. M. R. thanks the University Grant Commission (UGC) for providing a Junior Research Fellowship. D. Mehta thanks the Department of Biotechnology (DBT), India, for providing a Senior Research Fellowship.

References

1 K. Murotomi, A. Umeno, M. Shichiri, M. Tanito and Y. Yoshida, *Int. J. Mol. Sci.*, 2023, **24**, 2739.

2 G. Cui, S. Dong, C. Sui, T. Kakuchi, Q. Duan and B. Feng, *Int. J. Polym. Mater. Polym. Biomater.*, 2022, **71**, 109–115.
3 S. Yang, Y. Liu, T. Wu, X. Zhang, S. Xu, Q. Pan, L. Zhu, P. Zheng, D. Qiao and W. Zhu, *J. Med. Chem.*, 2025, 1.
4 Q. Dong and Z. Jiang, *Inorganics*, 2024, **12**, 331.
5 Y. Chen, Y. Deng, Y. Li, Y. Qin, Z. Zhou, H. Yang and Y. Sun, *ACS Appl. Mater. Interfaces*, 2024, **16**, 21546–21556.
6 C. Feng, Y. Wang, J. Xu, Y. Zheng, W. Zhou, Y. Wang and C. Luo, *Pharmaceutics*, 2024, **16**, 1582.
7 N. K. Panchal and E. P. Sabina, *Food Chem. Toxicol.*, 2023, **172**, 113598.
8 T. Pirmohamed, J. M. Dowding, S. Singh, B. Wasserman, E. Heckert, A. S. Karakoti, J. E. King, S. Seal and W. T. Self, *Chem. Commun.*, 2010, **46**, 2736–2738.
9 S. Singh, T. Dosani, A. S. Karakoti, A. Kumar, S. Seal and W. T. Self, *Biomaterials*, 2011, **32**, 6745–6753.
10 L.-Y. Tsai, K.-T. Lee and T.-Z. Liu, *Free Radicals Biol. Med.*, 1998, **24**, 732–737.
11 M. B. Bogdanov, L. E. Ramos, Z. Xu and M. F. Beal, *J. Neurochem.*, 1998, **71**, 1321–1324.
12 H.-A. Arab, R. Jamshidi, A. Rassouli, G. Shams and M. Hassanzadeh, *Brit. Poult. Sci.*, 2006, **47**, 216–222.
13 D. A. Parks and D. N. Granger, *Am. J. Physiol.: Gastrointest. Liver Physiol.*, 1983, **245**, G285–G289.
14 V. Vanasco, P. Evelson, A. Boveris and S. Alvarez, *Chem.-Biol. Interact.*, 2010, **184**, 313–318.
15 K. Murotomi, A. Umeno, M. Yasunaga, M. Shichiri, N. Ishida, H. Abe, Y. Yoshida and Y. Nakajima, *Free Radical Res.*, 2015, **49**, 133–138.
16 A. Filippi, F. Liu, J. Wilson, S. Lelieveld, K. Korschelt, T. Wang, Y. Wang, T. Reich, U. Pöschl and W. Tremel, *RSC Adv.*, 2019, **9**, 11077–11081.
17 Y. Ogawa, T. Kawaguchi, M. Tanaka, A. Hashimoto, K. Fukui, N. Uekawa, T. Ozawa, T. Kamachi and M. Kohno, *J. Clin. Biochem. Nutr.*, 2023, **73**, 1.
18 T. O. Shekunova, L. A. Lapkina, A. B. Shcherbakov, I. N. Meshkov, V. K. Ivanov, A. Y. Tsivadze and Y. G. Gorbunova, *J. Photochem. Photobiol., A*, 2019, **382**, 111925.
19 M. Bancirova, *Luminescence*, 2011, **26**, 685–688.
20 K. C. Das and H. P. Misra, *Mol. Cell. Biochem.*, 2004, **262**, 127–133.
21 D. Mehta, P. Sharma and S. Singh, *Colloids Surf., B*, 2023, **231**, 113531.
22 R. Regmi, R. Tackett and G. Lawes, *J. Magn. Magn. Mater.*, 2009, **321**, 2296–2299.
23 G. Wang, Q. Mu, T. Chen and Y. Wang, *J. Alloys Compd.*, 2010, **493**, 202–207.
24 S. Deshpande, S. Patil, S. V. Kuchibhatla and S. Seal, *Appl. Phys. Lett.*, 2005, **87**, 2.
25 C. Korsvik, S. Patil, S. Seal and W. T. Self, *Chem. Commun.*, 2007, 1056–1058.
26 J. Duan, S. Chen, S. Dai and S. Z. Qiao, *Adv. Funct. Mater.*, 2014, **24**, 2072–2078.
27 N. Yadav and S. Singh, *Emergent Mater.*, 2021, 1–13.
28 A.-N. Chowdhury, M. S. Azam, M. Aktaruzzaman and A. Rahim, *J. Hazard. Mater.*, 2009, **172**, 1229–1235.
29 F. Ducrozet, A. Sebastian, C. J. G. Villavicencio, S. Ptasinska and C. Sicard-Roselli, *Phys. Chem. Chem. Phys.*, 2024, **26**, 8651–8657.
30 Y. Xue, Q. Luan, D. Yang, X. Yao and K. Zhou, *J. Phys. Chem. C*, 2011, **115**, 4433–4438.
31 S. Duanghathaipornsuk, F. A. Alateeq, S. S. Kim, D.-S. Kim and A. C. Alba-Rubio, *Sens. Actuators, B*, 2020, **321**, 128467.
32 H. Tamura and H. Ishikita, *J. Phys. Chem. A*, 2020, **124**, 5081–5088.
33 C. Xu and X. Qu, *NPG Asia Mater.*, 2014, **6**, e90.
34 D. R. Learman, B. M. Voelker, A. S. Madden and C. M. Hansel, *Front. Microbiol.*, 2013, **4**, 262.
35 R. Singh and S. Singh, *Colloids Surf., B*, 2015, **132**, 78–84.